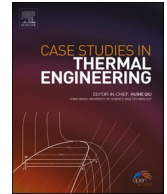




ELSEVIER

Contents lists available at [ScienceDirect](https://www.sciencedirect.com)

Case Studies in Thermal Engineering

journal homepage: www.elsevier.com/locate/csite

Flame characteristics of a high-pressure LOX/H₂ rocket combustor with large optical access

Jan Martin^{*}, Wolfgang Armbruster, Robert Stützer, Stephan General, Bernhard Knapp, Dmitry Suslov, Justin Hardi

German Aerospace Center (DLR), Institute of Space Propulsion, Im Langen Grund, Hardthausen am Kocher, Germany

ARTICLE INFO

Keywords:

Rocket engine
Sub-/supercritical combustion
Optical access
Liquid oxygen
Hydrogen
Single-injector

ABSTRACT

Hot fire tests were performed with a newly developed single-injector research combustor featuring a large optical access (255 × 38 mm) for flame imaging. Within these tests the propellant combination of liquid oxygen and cold gaseous hydrogen (LOX/H₂) has been used at chamber pressures up to 70 bar and ratios of oxidizer to fuel (ROF) at the main injector of 3.4–6. The large optical access enabled synchronized flame imaging using OH* and blue radiation wavelengths covering an area of the combustion chamber from the injection plane to shortly before the contraction section of the nozzle. High-speed flame imaging was realized for three different operating conditions. Combined with data from temperature, pressure and unsteady pressure sensors high-quality validation data for numerical modeling has been gained. Several key dimensions of the flame topology were extracted from the imaging. The change in flame topology in response to different operating conditions is consistent with expectations from the literature, in particular the dependence of flame opening angle on injection momentum flux ratio. Using OH* imaging for such topology measurements was found to have less uncertainty than with blue radiation imaging.

1. Introduction

Liquid propellant rocket engines (LPREs) are a key technology of world-wide launcher propulsion. Among the various liquid propellant combinations the cryogenic propellant combinations liquid oxygen with hydrogen (LOX/H₂) and Methane (LOX/CH₄) are of special interest due to their high performance. The oxygen-hydrogen propellant combination offers the highest specific impulse under all flown chemical propellants [1,2]. Therefore, LOX/H₂ plays an important role in current launcher developments. For example, the European Ariane 6 completely relies on LOX/H₂ rocket engines, apart from their solid propellant rocket boosters [3]. Moreover, the European space industry is already working on a new LOX/H₂ upper stage engine [4]. Other recent LOX/H₂ rocket engines, are the Japanese LE-9 [5], the Russian RD-0146 [6], the Chinese YF-77 [7] and in the US, the RS-25 for the Space Launch System, the RL-10C or the BE-3.

Injector design plays a key role in the development of LPREs. Stable flame anchoring, performance, combustion stability and the system pressure directly depend on injector geometry. For the propellant combination LOX/H₂ typically shear coaxial injectors are used [8,9]. Hereby, the liquid oxygen is injected through a central tube, the LOX post. The fuel with lower density is injected via a thin

^{*} Corresponding author.

E-mail address: jan.martin@dlr.de (J. Martin).

<https://doi.org/10.1016/j.csite.2021.101546>

Received 25 June 2021; Received in revised form 10 September 2021; Accepted 8 October 2021

Available online 9 October 2021

2214-157X/© 2021 The Authors. Published by Elsevier Ltd. This is an open access article under the CC BY-NC-ND license

(<http://creativecommons.org/licenses/by-nc-nd/4.0/>).

Nomenclature

u	velocity, m/s
ρ	density, kg/m ³
VR	velocity ratio of injected propellants
J	momentum flux ratio of injected propellants
l_{cc}	chamber length from injection plane to nozzle throat, mm
d_{throat}	diameter of nozzle throat, mm
T	temperature, K
P	static pressure, bar
p'	unsteady pressure, bar
$d_{o,or}$	diameter of LOX post orifice, mm
$l_{o,or}$	length of LOX post orifice, mm
$d_{o,po}$	diameter of LOX post, mm
$l_{o,po}$	length of LOX post, mm
$d_{o,ex}$	exit diameter of LOX post, mm
α	taper angle of LOX post, °
$l_{f,an}$	length of fuel annulus, mm
$d_{f,ex}$	exit diameter of fuel annulus, mm
$h_{f,gap}$	gap height of fuel annulus, mm
$d_{c,ex}$	exit diameter of window cooling annulus, mm
$h_{c,gap}$	gap height of window cooling annulus, mm
l_{re}	recess length of LOX post, mm
l_{window}	optical accessible length of window, mm
h_{window}	optical accessible height of window, mm
m_v	magnifying factor in vertical direction
h_{obj}	height of arbitrary object, mm
$h_{obj,im}$	height of arbitrary object at imaging plane, mm
\dot{m}	mass flow, kg/s
Tr	transmittance [%]
I_{ref}	reference image without window in optical path
I_{win}	image with window in optical path
$M_{tot, prim}$	total momentum of primary injector
ϵ_c	contraction ratio of nozzle

annular gap around the LOX post. Typical LOX post diameters for upper stage engines are in the range of 2–3 mm and 4–6 mm for main stage engines, respectively. The annulus height for the hydrogen is between 0.5 and 2 mm [8,10–12].

Apart from oxidizer-rich staged combustion engines, the oxygen injection temperatures are typically in the range of 94–100 K [11, 12]. Therefore, the oxygen is in the liquid state at injection. In European industrial engines, the hydrogen injection temperature is between 100 and 200 K, depending on the engine cycle. The hydrogen is always a supercritical fluid at injection.

The atomization and mixing of shear coaxial injectors are driven by the shear forces resulting from the velocity difference between the injected propellants. For that reason, the injection velocity ratio (VR) defined by equation (1) is an important design parameter for shear coaxial injectors.

$$VR = \frac{u_{H_2}}{u_{O_2}} \quad (1)$$

Typical oxygen injection velocities are between 10 and 30 m/s [1,9–12] and hydrogen injection velocities range from 150 to 360 m/s [1,9–11]. These values lead to velocity ratios of 8–39 in past rocket engines [11]. However, modern LOX/H₂ engines are usually characterized by velocity ratios of 10–20 [1,8,10,11]. An complementary design parameter is the momentum flux ratio (J), see Eq. (2):

$$J = \frac{\rho_{H_2} u_{H_2}^2}{\rho_{O_2} u_{O_2}^2} \quad (2)$$

Since the injectors impact the performance and the stability of the engine, they have to be designed with care and tested in sub-scale experiments, before they are placed in the actual full-scale rocket engine. However, this approach requires a lot of resources. Today, the development of new rocket engines occurs during an era of increased competition. Driven by the need for more cost effective and reliable rocket engines together with the rapidly growing computational resources, the use of CFD simulations in the development process of new rocket engines becomes more and more important. Consequently, the main focus in the development of new concepts, or upgrades to previous designs, has been shifting from verification through full-scale testing to simulations [9].

Numerical studies of the combustion processes of cryogenic propellants improved the understanding of the thermo and fluid

dynamic effects in highly turbulent, reactive flow fields at elevated pressures [13–17]. Numerical investigations thereby cover different aspects in the rocket combustion chamber, such as the general combustion processes and flame behavior at representative conditions [13,17–20], analysis of heat transfer [21–26], simulation of the ignition process [27], flame dynamics and combustion instabilities [14,16,28–32] or the investigation of new types of injectors [23,33,34]. The highly turbulent processes in liquid propellant combustion chambers include large thermal gradients from cryogenic fluids up to temperatures from more than 3500 K, real gas effects and combustion of non-premixed diffusion flames. Moreover, the combustion can be sub- or supercritical, depending on whether the chamber pressure is below or above the critical pressure of oxygen (50.4 bar). Past research at supercritical pressures showed that before droplets can be formed, the oxygen is rapidly heated up by the surrounding fuel and hot gas [10,17,35–37] and therefore undergoes a process, which is called pseudo-boiling [17]. This implies further challenges for the simulations, because for subcritical pressure droplet atomization, vaporization and combustion needs to be modeled, whereas for supercritical pressures, models are required which can accurately model the pseudo-boiling of oxygen as well as the mixing and combustion of two supercritical fluids [17]. For the given reasons, modeling of the processes in rocket engines at representative conditions still presents a challenge for the numerical tools today. Hence, there is an ongoing need for more experimental data suitable to validate the models of injection and combustion at these conditions [9,19].

Recent LOX/CH₄ test cases of TU Munich [38] attracted a lot of attention among the international rocket combustion modeling groups. A systematic comparison of the obtained simulation results, revealed that there are significant deviations between the modeling results themselves and also compared to the experiments [38,39]. The successful test case for LOX/CH₄ showed that this approach can help to improve the numerical tools.

Due to the extreme conditions inside rocket combustion chambers, also the experimental diagnostics are limited. The most common measurements include thermocouples near the wall and pressure measurements. In addition, non-intrusive flame visualization plays an important role in the validation of CFD simulation results within rocket propulsion. With sufficient temporal and spatial resolution, two-dimensional imaging can provide significant information about the dynamic behavior of combustion [40]. Windowed combustion chambers with a single coaxial injector have been used for injection and combustion studies at representative conditions. Optical access has provided a wealth of information on the characteristics of injection and flame topology. Several LOX/H₂ experiments with flame visualization have been published [37,41–47].

For hydrogen rocket combustion the most well-known test cases, which have been modeled by several international researchers are the experiments at the Mascotte test bench [15,16,18,19,48], the Penn State combustor [19,24,48,49] and the DLR combustor BKC [13,20,50,51]. However, to the author's knowledge there exists no LOX/H₂ test case with a representative main stage size injection element that allows optical high-speed diagnostics of the full-length flame visualization at representative operating conditions including sub- and supercritical chamber pressures. The BKC combustor, which has been used to visualize LOX/H₂ and LOX/CH₄ combustion [9,20,37,52,53], has 100 mm long windows. Recently, Suslov et al. placed the window at different axial positions in the combustion chamber. By that approach the authors were able to put together a full-length flame visualization by mean images of repeated test runs with similar operating conditions [9]. While this approach can be applied to time averaged flame images to investigate the flame length in dependence of operating conditions, the composite image suffers from a degree of disjointedness. For example, it is not possible to investigate flame dynamics over the full chamber length coherently with this approach.

In order to overcome a majority of the described limitations of existing research rocket combustion chambers with optical access, a new experiment, designated combustor model 'N' (abbr. BKN), has been developed at the Institute of Space Propulsion. During the development of this particular experiment, focus was placed on its suitability for validation purposes and to obtain well-defined boundary conditions. Therefore, the experiment is extensively equipped with conventional diagnostics, such as thermocouples and pressure sensors. The most relevant feature, however, is the large optical access window with a length of 255 mm, which allow the world's first full-length flame visualization from a main-stage engine-scaled injector with the corresponding mass flows. The window's inner surface matches the contour of the combustion chamber wall to minimize disturbance to the symmetry of the flow field in the combustion chamber.

The implemented injector is of the classic shear coaxial type compatible with the use of both hydrogen or methane as the fuel. The injector is more optimized for methane injection than for hydrogen, resulting in the relatively high ranges of J (22–95) and VR for hydrogen in this work compared to those typically found in similar experimental LOX/H₂ rocket combustors with flame visualization (0.15–35; [37,41,43–47]). Woodward et al. [42] performed experiments in the J number regime between 22 and 50, but with a smaller element, reduced mass flows, and limited optical accessibility.

In this work, experiments were performed with BKN to characterize the topology of the LOX/H₂ flame at chamber pressures both sub- and supercritical for oxygen. High-speed flame emission imaging of both UV- and blue-wavelength regimes was implemented. To the authors' knowledge, this work is the first to present blue imaging of the full extent of a full-scale, high-pressure, cryogenic flame.

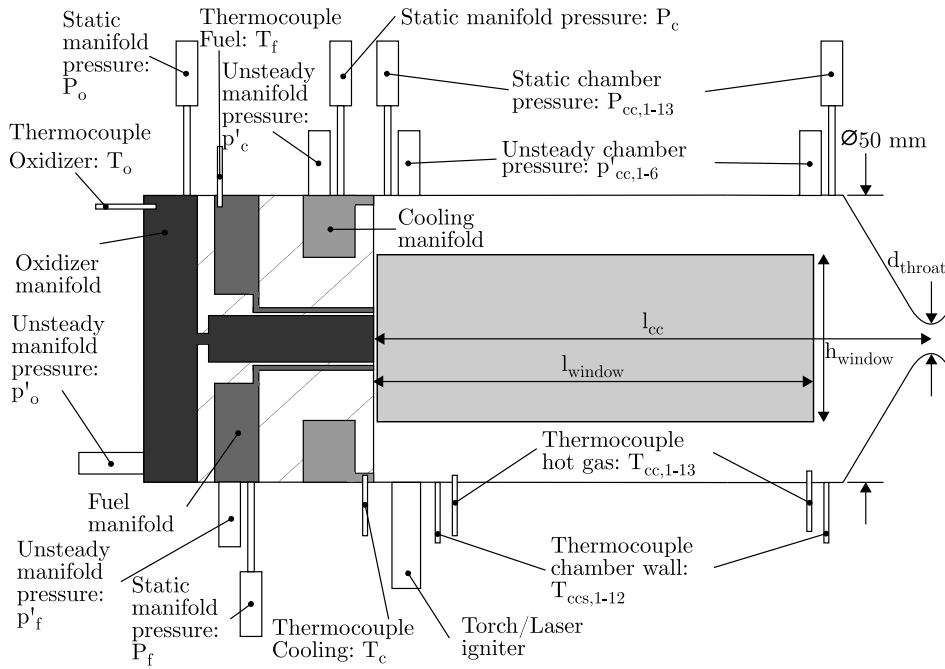
This paper begins by describing the experimental setup and also the measurement technique. Then, the optical as well as the conventional data are analyzed to extract key dimensions of the flame topology, and to define the wall pressure and temperature conditions under which the visualization was performed. The influence of different operating conditions on the flame topology will be discussed, and the utility of each type of imaging for this kind of study will be compared and contrasted.

2. Experimental method

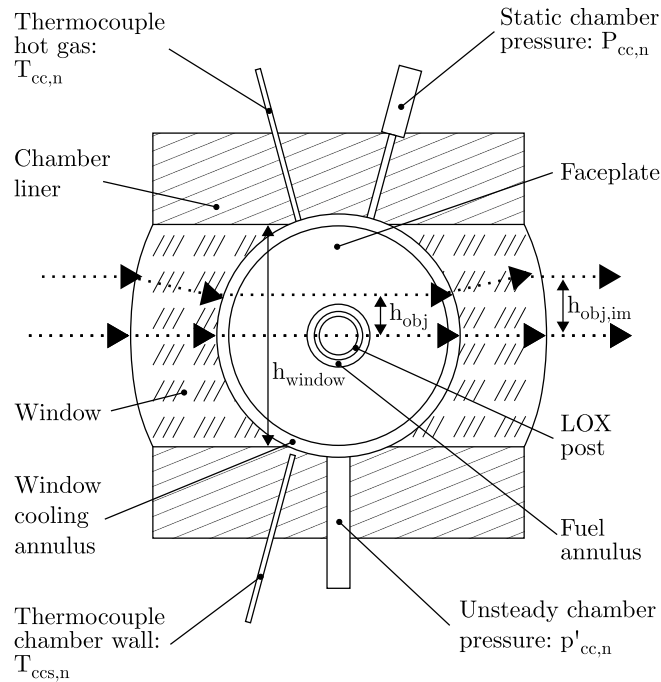
2.1. Combustion chamber

The hot-fire tests presented in this work were conducted at the European Research and Technology Test Facility P8 [54] for

cryogenic rocket engines with the DLR research combustion chamber 'N'. BKN consists of a single-element injector head, an optical chamber segment with 50 mm diameter and a convergent divergent nozzle. An illustration of the combustor configuration is given in Fig. 1(a). The overall length (l_{cc}) of the combustion chamber from faceplate to the nozzle throat with a diameter (d_{throat}) of 16.9 mm is 362 mm. The geometry of the optical access will be addressed in detail in the next paragraph.



(a) Combustion chamber schematic



(b) Combustion chamber cross section

Fig. 1. Experimental combustion chamber configuration.

Since one of the experiment’s purposes is to provide detailed information about the flow and boundary conditions during operation in addition to parameters like chamber pressure and mass flow rates, it is densely equipped with sensors. Therefore at least one thermocouple, static pressure sensor and unsteady pressure sensor are mounted to the manifolds for LOX (T_o, P_o, p'_o), cold gaseous hydrogen (T_f, P_f, p'_f) and window cooling (T_c, P_c, p'_c). The same kind of measurement devices are also available in the chamber segment. Thermocouples with a sampling rate of 100 Hz are mounted to the chamber segment in two different ways. The values given in brackets correspond to the sensor positioning as distance from the faceplate with respect to the inner diameter of the LOX post ($\frac{l}{d_{o,po}}$). In the first case 13 thermocouples ($T_{cc,1-13}$) protrude approximately 0.1 mm (0.02) into the chamber and are distributed every 20 mm (3.64) between 4.5 mm (0.82) and 244.5 mm (44.45) downstream of the faceplate. A further 12 thermocouples ($T_{ccs,1-12}$) are mounted within the walls with contact to the structure, 1 mm (0.18) back from the combustion chamber wall and also placed every 20 mm (3.64) between 34.5 mm (6.27) and 254.5 mm (46.27) downstream of the faceplate. Static pressure ($P_{cc,1-13}$) sampled at a rate of 100 Hz can also be provided at 13 axial positions every 20 mm (3.64) between 4.5 mm (0.82) and 244.5 mm (44.45) downstream of the faceplate. Six flush mounted unsteady pressure sensors are positioned at distances of 34.5 mm (6.27), 84.5 mm (15.36), 94.5 mm (17.18), 134.5 mm (24.45), 164.5 mm (29.91) and 234.5 mm (42.64) downstream of the faceplate. The signals are sampled at a rate of 100 kHz with a 30 kHz second order anti-aliasing filter and have a measurement range of ± 30 bar. The implementation of each type of sensor is indicated in Fig. 1(b).

LOX and H₂ are injected through a shear coaxial injection element with a tapered LOX post. Additional film cooling (H₂) reducing the heat load applied to the optical access is also injected via an annular gap between chamber wall and faceplate. Both injection systems are illustrated in Fig. 2. The dimensions of the injection system are given in Table 1.

Combustion is started by either a torch or a laser ignition system. Both methods can be applied due to a modular ignition port.

2.2. Optical access

In addition to the densely distributed measurement devices BKN also features a Full-Length Optical Window (FLOW). The FLOW can be mounted to both sides of the chamber and enables optical access covering an area from the injection plane to shortly before the contraction section of the nozzle. The optical accessible length (l_{window}) of the window is 253.5 mm. The optical accessible height (h_{window}) with regard to the combustion zone is 38 mm.

A major improvement in comparison to previous optical combustion chambers, like BKC, is the contoured inner (and outer) surface to maintain the cylindrical combustion volume. While the radius of the inner surface is given by the chamber diameter, the radius of the outer surface is optimized to reduce vertical distortion of the images with respect to a light source producing parallel rays (Fig. 1 (b)). Therefore the combination of two contoured surfaces also enables the application of this window geometry for shadowgraph imaging. Hence a perfect compensation of the light rays’ deviation due to the cylindrical inner surface is not possible with a cylindrical outer surface, the remaining distortion was characterized. For this purpose a pattern with equidistant stripes was recorded with a monochrome digital camera (The Imaging Source DMK 33UX250 with ZEISS Milvus 100 mm 2.0 ZF.2) through the window. The pattern was back-illuminated by a LED light source (HARDsoft IL-106X) with a center wavelength of 528 nm and placed at a distance behind the window that corresponds to the distance between window and chamber axis when installed. These stripes cause local intensity extrema in the recorded images whose vertical positions can be determined. Reference images without the FLOW in the optical path showed a distance of 6 pixels. Fig. 3 illustrates a measurement with the FLOW in the optical path.

The detected extrema are indicated in the left part of Fig. 3 and the calculated distance between neighboring extrema in the right part. The resulting values range from 9 pixels along the center line of the window to approximately 12 pixels at the edge of the curved surface (center part of Fig. 3). Fig. 1 (b) illustrates this magnifying effect as a result of the rays’ refraction when passing through the boundary of the quartz window. The locally resolved vertical magnifying factor (m_v) can be easily computed comparing the distances

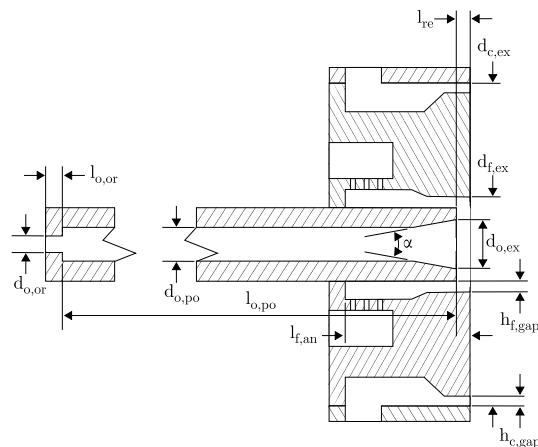


Fig. 2. Injection system configuration.

Table 1
Geometrical dimensions of injection systems.

Symbol	$d_{o,or}$	$l_{o,or}$	$d_{o,po}$	$l_{o,po}$	$d_{o,ex}$	α
Unit	mm	mm	mm	mm	mm	°
Value	2.2	4.0	5.5	127.0	6.3	8
Symbol	$l_{f,an}$	$d_{f,ex}$	$h_{f,gap}$	$d_{c,ex}$	$h_{c,gap}$	l_{re}
Unit	mm	mm	mm	mm	mm	mm
Value	34.5	8.2	0.5	50.0	1.0	4.0

between maxima in the recorded image ($h_{obj,im}$) at the imaging plane with those of a reference image without optical access and thus no distortion (h_{obj}).

$$m_v = \frac{h_{obj,im}}{h_{obj}} \tag{3}$$

The aforementioned pixel values between the maxima correspond to magnification factors of about 1.5–2.0. The exact magnification factors can be calculated by normalizing the distances with the mean value of non-distorted image regions and subsequently fit a polynomial of degree 2 to the distorted image part

$$m_v(d_{center}) = a_0 + a_1 d_{center}^2, \tag{4}$$

where d_{center} describes the distance from the center-line normalized by the half height of the window. This yields to coefficients of 1.5 for a_0 and 0.5 for a_1 . In order to correct the distortion, the height of each row in the recorded image is scaled by the reciprocal of the according magnification factor. The result can be seen in Fig. 4. As expected, the distance between extrema from the reference image of the window now corresponds to the value of the undistorted image areas (see Fig. 3).

The transmittance Tr of the window is another important factor for elimination of possible uncertainties introduced by the flame contoured inner and outer surface. For this purpose, two images of the background pattern were recorded with identical camera settings. One image (I_{ref}) only shows the background, while the other one (I_{win}) also contains the window in the optical path. By calculating the quotient of the image intensities

$$Tr = \frac{I_{win}}{I_{ref}}, \tag{5}$$

one can draw conclusions about the transmittance of the window. Prior to calculating the quotient, the images were smoothed with a Gaussian filter to remove high-frequency spatial information from the background pattern. The resulting spatially resolved transmittance of the window can be seen in Fig. 5. Since the brightness of both images generally decreases towards the edges, the free aperture of the window was corrected for vertical distortion with the above-mentioned method before calculating the quotient and subsequently reinserted into the image.

This ensures that identical regions of the images are compared to each other. As can be seen, the resulting transmittance in this area is relatively constant. There is only a slight drop in transmittance towards the upper and lower edge of the area, from about 93% along the center line of the window to 90% at the edge. This is probably due to a change in the angle of incidence of light rays on the curved surface of the window.

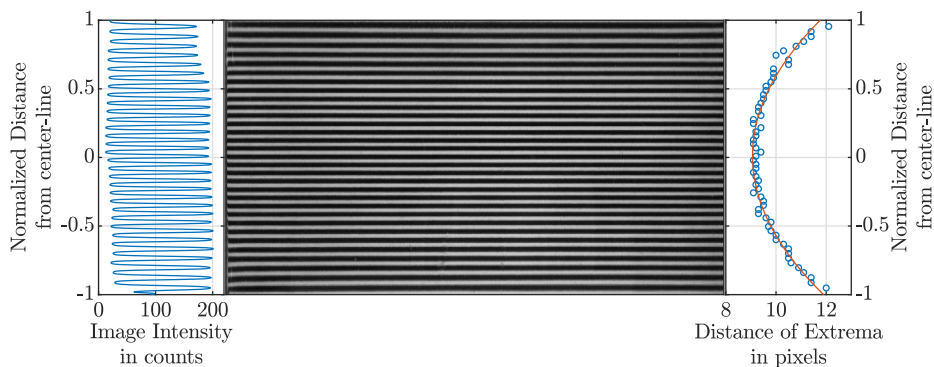


Fig. 3. Characterization of the window’s vertical distortion with a background of equidistant stripes. Center: Captured picture with the FLOW in optical path. Left: Intensity distribution of the image in vertical direction along the center. Right: Calculated distance of neighboring extrema and related fits.

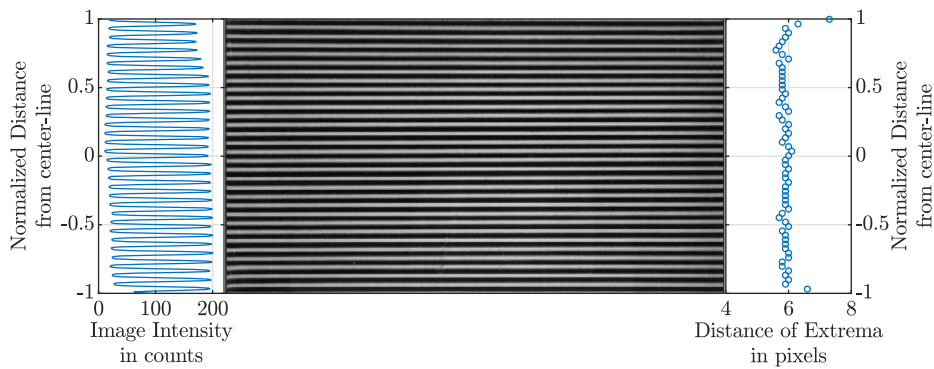


Fig. 4. The recorded image was corrected for vertical distortion with the calculated magnification function. Left: Corrected intensity distribution. Right: The intensity extrema are equally spaced now for the free aperture of the window.

2.3. Flame radiation imaging

Two flame emission aspects were investigated using high-speed imaging: The ultraviolet (UV) as well as the visible (blue) regime (BR). The infrared (IR) radiation also contributes to the emission spectrum. However, due to its complexity and general indistinguishability from background emission of the hot combustor walls it is not considered for analysis. The UV-Vis regime has its origin in the radiation of molecules that are excited by chemical reactions (chemiluminescence) and thermal collisions. For hydrogen-oxygen flames at 50 bar pressure, below a temperature of approximately 2700 K, chemiluminescence exceeds thermal excitation [55]. Above this transition temperature, thermal excitation is primarily responsible for OH* formation. Due to the exponential increase regarding temperature, thermal excitation clearly dominates the OH* production above a temperature of 3000 K at which chemiluminescence is already negligible [56].

In hydrogen flames, as applied in this test case, only molecules containing hydrogen and oxygen atoms are present. In particular two molecule species contribute to the UV-Vis regime of the spectrum: The excited hydroxyl radical (OH*) with its intense emission bands around 310 nm and the excited H₂O₂ molecule which is suspected to strongly contribute to the broad spectral continuum with a maximum between 430 and 450 nm [57]. Equation (6) describes the path for OH* production according to Kathrotia et al. [58] and Leo et al. [59]. The constituent *M* is an arbitrary species in the system that is necessary for conservation of momentum. Formation of the H₂O₂* radical is depicted in equation (7) as described by Padley [60]. Other possible radiation sources, such as the Schumann-Runge lines of the O₂ molecule, can be neglected [61].

Both UV and blue spectral regimes respond to increasing pressure with a higher emissivity. However, while for ambient conditions the UV radiation is predominant, a pressure of more than 60 bar results in a visible (blue) radiation that is the most intense spectral feature [55].



The physical origin of the OH* radiation around 310 nm is the transition from the first electronically excited state ($A^2\Sigma^+$) to the ground state ($X^2\Pi$). Both energy levels correspond furthermore to several vibrational and rotational states. Since the transition probability from the excited state *i* to the ground state *j* is a constant (Einstein-coefficient $A_{j \rightarrow i}$), the emitted number of photons from within a unit volume is directly proportional to the amount of molecules in the excited state [62,63].

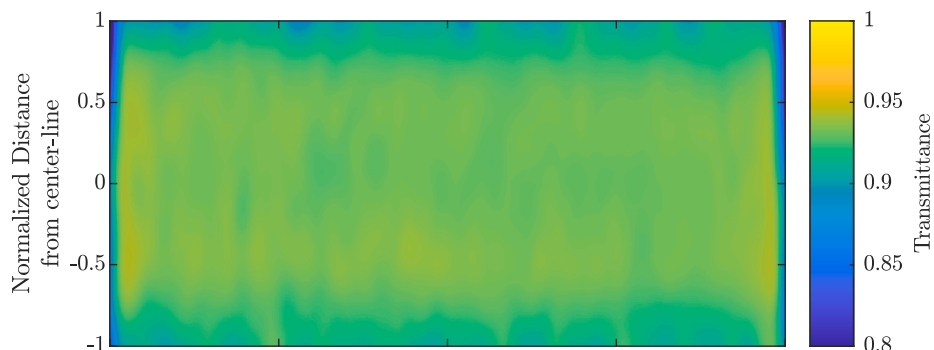


Fig. 5. Calculated transmittance of the window.

Imaging of OH* radiation is a two-dimensional line-of-sight integrated measurement. Therefore, the attenuation along the optical path has also to be discussed. The hydroxyl radical has the ability to absorb photons that were emitted by other OH* molecules from within the flame core. This process is referred as self-absorption. Hence, imaging methods that take advantage of UV radiation can only visualize the nearest surface of hydrogen flames. For visible (blue) light, on the other hand, the hydrogen flame appears clearly more transparent. Thus the camera sensor collects nearly all photons of $\lambda = 450$ nm that are emitted along the line of sight.

2.4. Optical setup

Flame and combustion visualization of the ultraviolet and blue optical regime was carried out using two synchronously and coaxially recording high-speed camera systems. A dichroic mirror (transparent for visible light and reflective for UV radiation) split the optical axis for obtaining an identical field of view for both camera systems. Compressed-air cooled metal housing prevented the optical setup from overheating and mechanical damage. The visible (blue) flame emission was recorded by a Photron® Fastcam SA-Z type 2100K-M-64G camera model. Its proprietary design advanced CMOS image sensor has an active area of 20.48×20.48 mm, and 1024×1024 pixels respectively. The RAM capacity of 64 GB allows the storage of 43,682 frames at full resolution. Flame emission, without background illumination, was recorded with up to 20,000 fps and an exposure time of 7.5 μ s. A Carl Zeiss® Makro-Planar ZF.2 lens with $f = 100$ mm and an aperture of 2.8 was used, equipped with a band pass filter (CWL: 436 nm; FWHM: 10 nm; T(436 nm): 50%) from Andover Corporation (Fig. 6, right).

Ultraviolet radiation (OH* chemiluminescence) was recorded using an image intensified Photron® Fastcam SA-X2 type 480K-M4 high-speed camera, also equipped with an identical proprietary design advanced CMOS image sensor. Frame rates of 3000 Hz–20,000 Hz were applied. The UV radiation was converted into visible light using a Hamamatsu® image intensifier, model C10880 GHD1101, which was attached to the camera's lens mount. Gate width and gain were set for optimal image quality. A Nikon® UV-Nikkor $f = 105$ mm lens with an aperture of 4.5 was used, equipped with a UV band pass filter (CWL: 306.8 nm; FWHM: 10 nm; T(306.8 nm): 64%) (Fig. 6, left).

2.5. Operating conditions

In this initial campaign with BKN tests were conducted at chamber pressures up to 70 bar and ROFs at the main injector up to 6. Data of three LPs originating from two test runs are presented in this work.

Both tests are presented in Fig. 7 and in Fig. 8. The test sequences are described with traces of the static chamber pressure P_{cc} , LOX injection temperature T_o , hydrogen injection temperature T_f , and ratio of oxidizer to fuel mass flow rate ROF. For all LPs the unsteady pressure amplitude was below 2.5% of the mean chamber pressure. These traces of parameters describe the performed sequence of operating conditions. The European Research and Test Facility P8 allows to regulate the mass flows with control valves and thus it is possible to have a test with several load points within one test run. The control valves can either be operated by setting valve positions in an open-loop configuration or in combination with the feedback of the calibrated flow meters as a closed-loop configuration. The duration of each load point is at least about 3 s, which allows a steady-state thermal equilibrium condition to be reached. The intervals used for extracting the data for the three LPs (LP1: 8–8.5 s in Test 1, LP2: 18–18.5 s in Test 1, LP3: 18–8.5 s in Test 2) are highlighted in gray. For all three LPs high-speed imaging of OH* and blue radiation with 20 kfps is available.

Table 2 summarizes the steady state test condition and the injections condition for all three load points. The data are mean values from a sample period of 0.5 s.

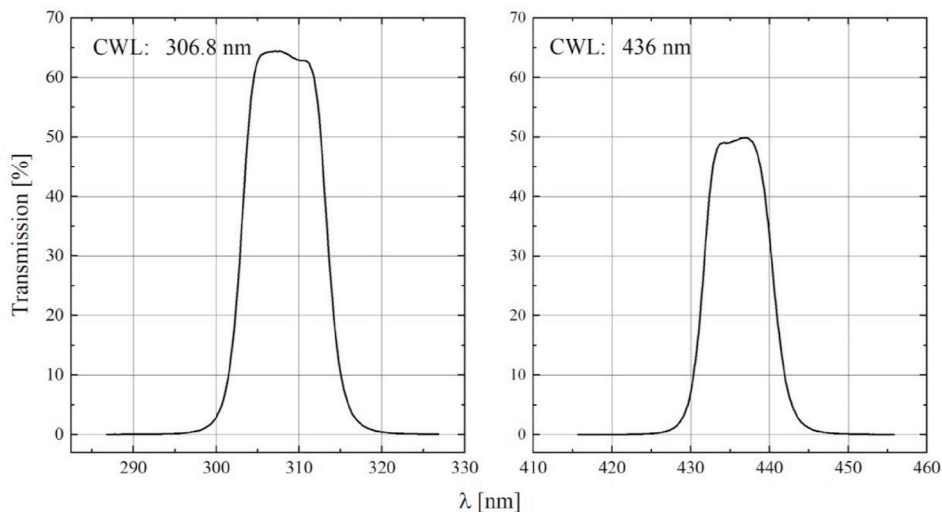


Fig. 6. Wavelength dependent transmission of the optical bandpass filter with a center wavelength of 306.8 nm (left), and 436.0 nm (right).

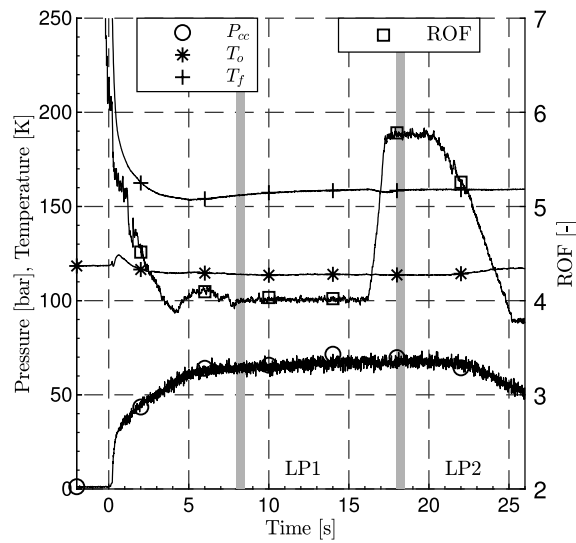


Fig. 7. Test Sequences of first test with operating conditions and gray highlighted intervals used for extracting the data for load point 1 and load point 2.

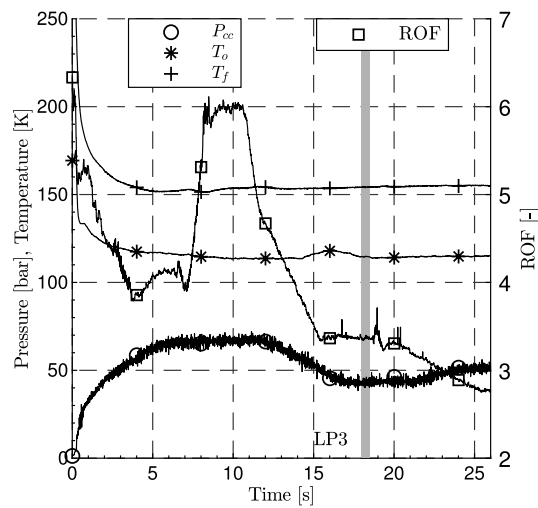


Fig. 8. Test Sequences of second test with operating conditions and gray highlighted interval used for extracting the data for load point 3.

Table 2
Steady state and injection conditions for all three load points.

Parameter	Unit	Load point			Uncertainty
		1	2	3	
P_{cc}	bar	64.3	67.7	43.0	$\pm 1.1\%$
ROF	—	4.0	5.8	3.4	$\pm 5\%$
\dot{m}_o	kg/s	0.328	0.345	0.234	$\pm 3\%$
\dot{m}_f	kg/s	0.082	0.060	0.070	$\pm 3\%$
\dot{m}_c	kg/s	0.199	0.230	0.100	$\pm 3\%$
T_o	K	115	114	115	$\pm 3.5 K$
T_f	K	165	167	161	$\pm 3.5 K$
T_c	K	296	303	306	$\pm 2.0 K$

3. Results and discussion

The flames' characteristics within the chamber and the resulting boundary conditions to the chamber will now be presented for all three LPs.

Fig. 9 shows the flame radiation in the blue regime (bottom) and OH* (top) in the near-injector region for all three LPs. In all cases the flame seems to anchor at the LOX post tip as expected for combustion with the propellant combination LOX/H₂.

Single Frames, for both kind of radiation, are presented in Fig. 10 for LP1, Fig. 11 for LP2 and Fig. 12 for LP3. These images are giving an insight into the highly turbulent character of the flame. Further in each figure the flame radiation measurements are interrupted by small sections with nearly diminished intensity. This implies detachment of big pockets of combustion products at significantly earlier distances from the faceplate than the flame lengths calculated later from time-averaged images. It should be noted that Figs. 10–12 compare the same half of the flame in both OH* and blue radiation. The blue imaging in the lower half of the figures is a mirrored image of the upper half of the flame from the same instance as the OH* image.

The velocity ratio, the momentum flux ratio and the total injection momentum of the propellants at the main injector as important design parameters for injection elements are given in Table 3.

The reason for the high values of both parameters compared to past rocket engines can be found in the small gap height of the fuel annulus. The injection element was designed as a hybrid element optimized for methane but also useable for hydrogen as fuel, which results in high injection velocities of the hydrogen due to its low density.

Time averaged images, again for both kind of flame emission imaging over the whole duration of each LP and whole FLOW are illustrated in Fig. 13 for LP1, Fig. 14 for LP2 and Fig. 15 for LP3. From these, preliminary analysis of the injection parameters' influence on the flame's topology such as opening angle, flame width and length can be derived. Again the blue imaging is mirrored vertically in these figures for better comparability.

While OH* radiation suffers from high self-absorption, this is not the case for blue radiation. Therefore, the captured blue images can be considered to be line-of-sight integrated and thus justifies the application of an inverse Abel transformation to give cross-sectional information on the flame. Fig. 16 shows the inverse-Abel transformation of the time-averaged imaging of LP2, calculated according to Hansen and Law [64]. It can be seen that a great portion of the captured intensity for the first 40 mm is generated in the shear layer of the flame between the central oxygen jet and the coaxial hydrogen stream.

Next, flame opening angles were measured. Image processing steps for the flame angle extraction are shown in Fig. 17 for the OH* radiation in LP1. First a threshold based flame boundary detection algorithm is applied to a time averaged image for the corresponding LP. Then a binary image is derived from the detected flame. Finally, two polynomials of first order are fitted to the fuel exit diameter ($d_{f,ex}$) and the outer boundary of the flame within the specified region of interest. To avoid artifacts within the flame angle calculation caused by the nonlinear widening further downstream, the limit for all extracted angles has been set to 6.0% of the chamber length. This corresponds to 15.2 mm or a dimensionless distance of 2.77.

For the flame width, mean values of each row, and for the flame length, mean values of each column, were calculated. In this case, 75% of the peak intensity from the time averaged OH* and blue radiation images was used to define the flame width at three quarter maximum (FIW34M) and the flame length at three quarter maximum (FIL34M). It should be noted that for the latter case only the downstream limitation of the intensity at half maximum has been considered. Due to the low intensity in the near-injector region, with the FIL34M criterion a flame boundary is also detected in the upstream part of the flame. Because the flame anchors at the LOX post tip for all operating conditions this boundary has been neglected.

Table 3 also gives the opening angles based on the averaged OH* and blue images. Kendrick et al. found a greater opening angle for recessed injectors and explained this behavior by the increase of J number due to the constricted gaseous flow [65]. This is in good agreement with the angles extracted from OH* imaging within this work. A rise of the momentum flux ratio is accompanied by an

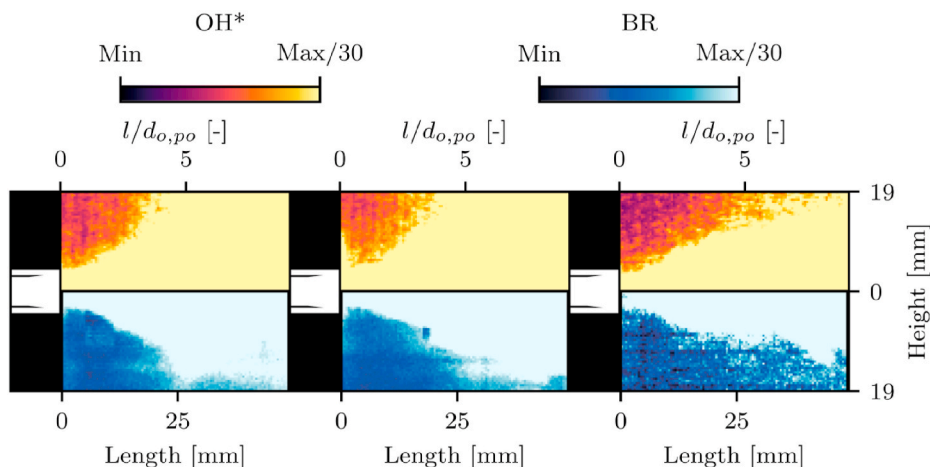


Fig. 9. Zoomed instantaneous flame radiation imaging (OH*/BR) of LP1-3 with focus on the injection plane.

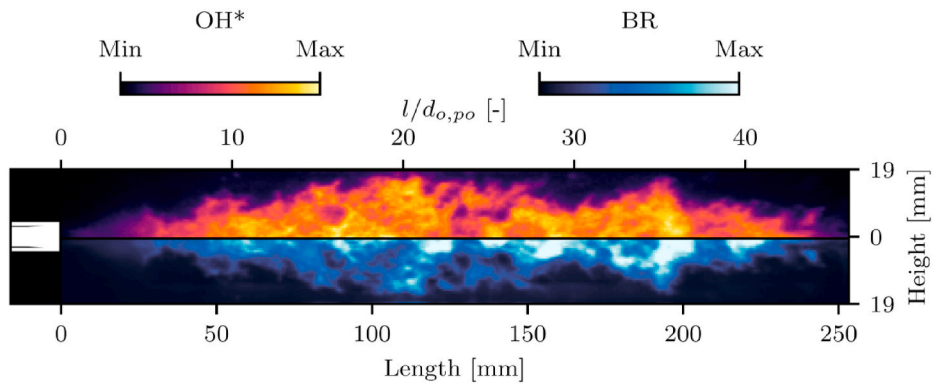


Fig. 10. Instantaneous flame radiation imaging (OH*/BR) of LP1.

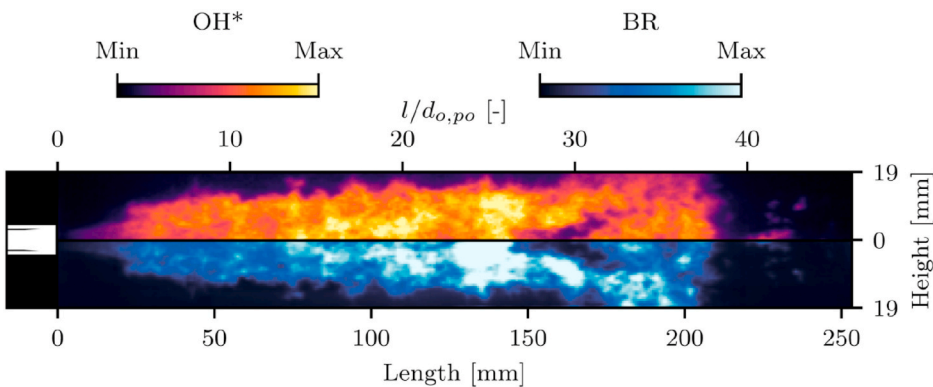


Fig. 11. Instantaneous flame radiation imaging (OH*/BR) of LP2.

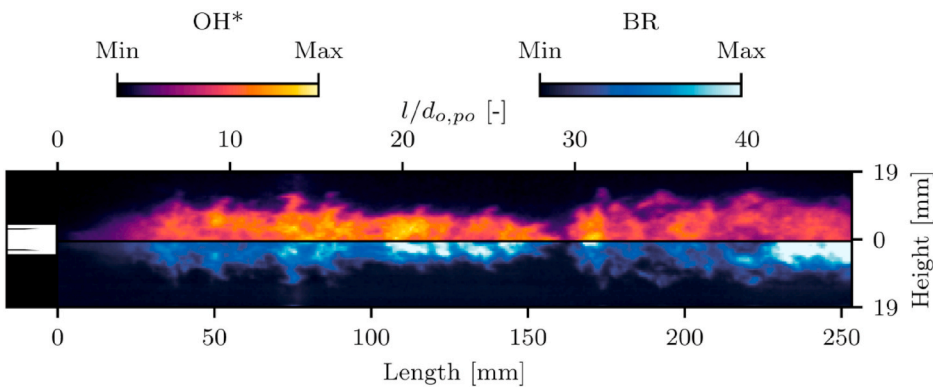


Fig. 12. Instantaneous flame radiation imaging (OH*/BR) of LP3.

increasing opening angle. For the blue radiation the same trend applies, although the extracted angles are consistently smaller.

The OH* images show far less variation in intensity within the flame region due to the high self-absorption at these wavelengths. The gradient at the boundaries is strong for all load points giving good consistency in the extraction of flame angles. In contrast, the blue images have weaker gradients in the flame boundary region, resulting in higher uncertainties in edge detection. For the extraction of all angles, two different thresholds have been applied. The first threshold has been chosen at the lower limit of intensity gradient detection. The second threshold has been set to the first local maximum of the intensity gradient development in direction to the center of the flame. The mean values of the resulting limit case angles is used to determine the range of uncertainty in angle measurement, and these are given as uncertainty values in Table 3.

The influence of J and VR on the flame width correlates similarly to the opening angle. Higher values of those injection parameters result in increased flame width for supercritical chamber pressures. However, the flame width for the subcritical LP3 is the smallest.

Table 3
Injection parameters and measured flame topology for all three load points.

Parameter	Unit	Load point			Uncertainty
		1	2	3	
VR		73	50	125	
J		47	22	95	
$M_{tot, prim}$	$\frac{kg}{ms^2}$	5198928	2741042	5394531	
		OH*			
Opening Angle	deg;	31.0	14.0	36.1	±3
Flame Width	mm	18.9	18.2	17.1	±0.18
Flame Length	mm	201.5	195.3	219.7	±0.34
		Blue radiation			
Opening Angle	deg;	28.2	4.6	29.6	±4.5
Flame Width	mm	13.7	13.3	13.3	±0.21
Flame Length	mm	223.6	211.4	237.8	±0.40

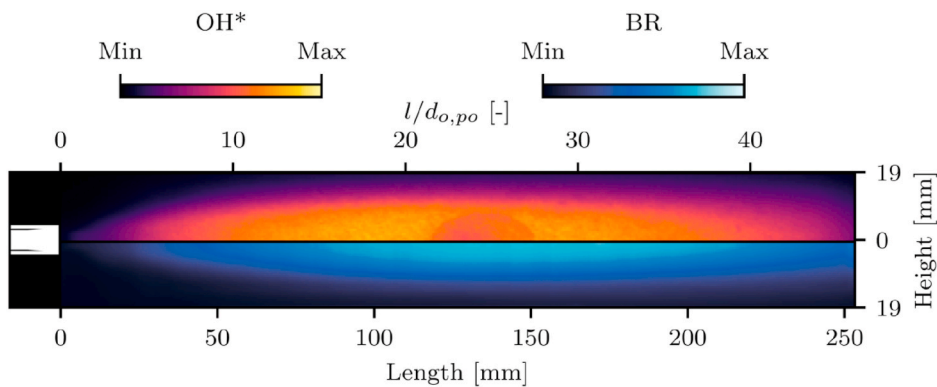


Fig. 13. Time-averaged flame radiation imaging (OH*/BR) of LP1.

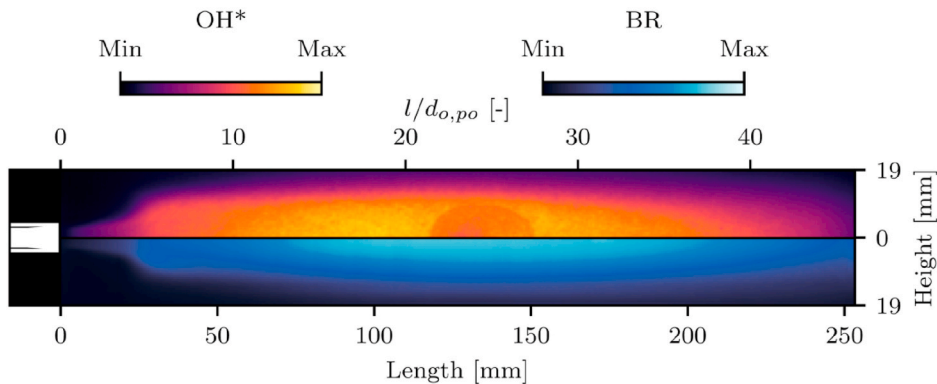


Fig. 14. Time-averaged flame radiation imaging (OH*/BR) of LP2.

The reason for this is unknown, but an explanation could be sought in the difference in propellant mixing processes at subcritical pressure, where surface tension at the oxygen-hydrogen interface plays a non-negligible role.

The relationship between J and VR and the flame length are unexpected. Previous investigations from Suslov et al. [9] with BKC found a shortening of the intact LOX core for higher J numbers and thus a shortened flame would be expected as well. Here, increased J is followed by a longer flame. Various explanations could apply. In the current experiment no measurement of the intact LOX core has been conducted but an estimation of the flame length by means of an intensity threshold is available. A direct relation between intact LOX core length and intensity of the flame emission can not be assumed. Furthermore an influence of the injected cooling mass flow on the flame cannot be excluded. Finally, the total momentum of the injected propellants should be considered as well. It is reasonable to

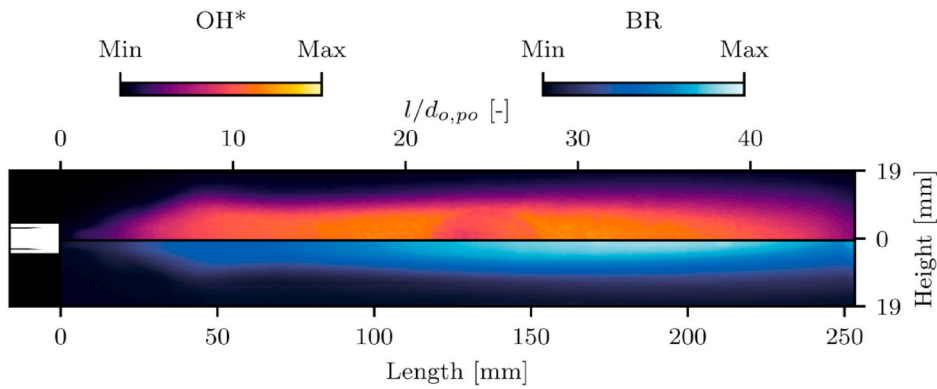


Fig. 15. Time-averaged flame radiation imaging (OH*/BR) of LP3.

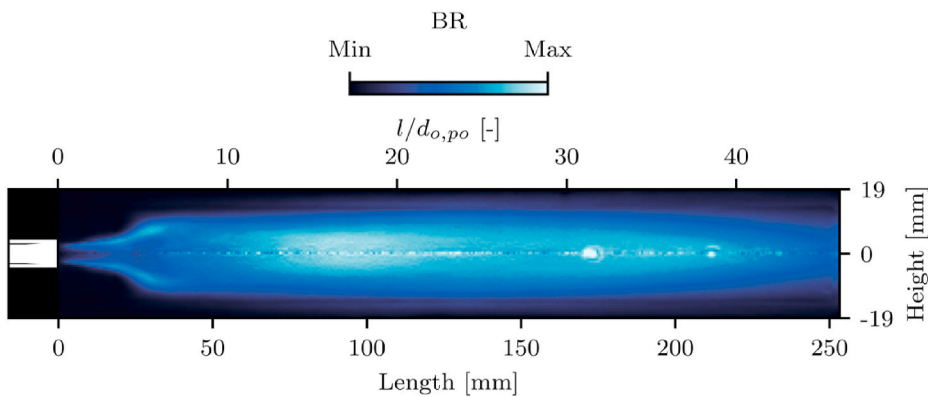


Fig. 16. Inverse-Abel transformation of time-averaged blue radiation imaging for LP2. (For interpretation of the references to colour in this figure legend, the reader is referred to the Web version of this article.)

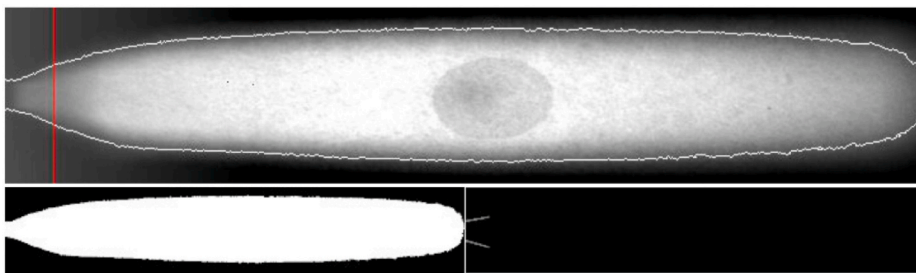


Fig. 17. Time-averaged flame radiation imaging (OH*) of LP1 with detected flame (top), binarized image of the detected flame (bottom left) and the extracted flame angle in the region of interest (defined by red rectangle). (For interpretation of the references to colour in this figure legend, the reader is referred to the Web version of this article.)

assume that a higher total momentum of the injected propellants results in an extension of the flame within the chamber.

The observed flame characteristics are qualitatively the same in both the OH* and blue radiation imaging in response to the injections conditions. Blue imaging tends to give a 15–20 mm longer flame with the FIL34M criterion.

The general flame topology can also be subdivided into two categories. The first category is a gradual linear widening of the flame and occurs at high momentum flux ratio, respectively low values of ROF. The second category is characterized by a widening which can be best described by an exponential increase of width with the length for high ROF and low momentum flux ratio.

The temperature distribution in all three LPs measured by the thermocouples protruding into the hot gas (T_{cc}) is shown in Fig. 18. A nearly identical linear rise of the temperature can be seen for all three LPs between 0 and 64.5 mm downstream of the injection plane before the measurements start to differ. The similar temperature distribution in the upstream part of the chamber is primarily defined by the injected window cooling film. From approximately 100 mm downstream the load points are distinguishable. The highest

temperatures are measured for LP2, which is to be expected since LP2 has the highest ROF (5.8) and therefore the highest equilibrium gas temperature.

All LPs have a stagnation of the temperature increase between 104.5 and 144.5 mm in common. This is speculated to be caused by an interaction of the flame from the main injector with the injected film cooling after expanding in the upstream part of the chamber. Numerical modeling would allow this effect to be investigated further. After this stagnation the temperature grows again asymptotically towards the final value which is approximately 900 K for LP1, 1100 K for LP2 and 850 K for LP3.

The temperature distribution in all three LPs measured by the thermocouples with contact to the chamber wall (T_{ccs}) is illustrated in Fig. 19. The temperature distribution here shows a roughly linear behavior for all three LPs between 0 and 194.5 mm downstream of the injection plane before switching to a more exponential temperature increase for the last three measurement locations. Here, the most downstream temperature measurement shows the highest value for LP3.

The pressure (P_{cc}) distribution (Fig. 20) within the chamber between 0 and 244.5 mm seems to stay constant along the chamber axis in all three LPs. This behavior was expected due to the high contraction ratio (ϵ_c) of the nozzle. High values for ϵ_c lead to nearly constant static pressure in the chamber while rapidly decreasing in the nozzle section.

4. Conclusions

Three different operating conditions met by a sub-scale rocket combustion chamber with large optical access were presented in this work. The propellant combination LOX/H₂ was injected through a shear coaxial injection element with relatively high momentum flux and velocity ratio regimes compared to most engines. For each load point the steady-state flame characteristics such as upstream opening angle, width and length were extracted from simultaneous radiation imaging filtered in the UV and blue wavelength ranges, respectively. Consolidation of these measurements with the axial development of temperature and pressure signals give well-defined information on the boundary conditions in the combustion chamber. The design of the combustor and application of diagnostics are intended to optimize its utility as a test case for validating numerical modeling of LOX/H₂ flames.

The influence of the momentum flux ratio and the velocity ratio on the flame's topology has been analyzed. Higher values of those injection parameters lead to a wider flame and steeper opening angle. These findings are in good agreement with the enhanced mixing due to increased J values proposed by literature. On the other hand, no consistent relation between flame length and J number was found in comparison to literature. The known correlations may not apply for the high momentum flux ratio regime investigated here. It is speculated that the total momentum of the injected propellants become more dominant. However, since correlations in literature usually refer to the intact LOX core length dependent of the momentum flux ratios, measurement of the intact LOX core length with shadowgraphy should be considered for future test activities. Instantaneous images of the flame revealed detachment of big pockets of combustion products from the flame anchoring inside the recess, presumably at the LOX post tip.

While hot gas temperatures were highest for a ratio of oxidizer to fuel of 5.8 and supercritical chamber pressures with respect to the oxygen, the highest value for the structural temperature occurred at a low oxidizer-to-fuel ratio (3.4) and sub-critical chamber pressures. Due to the high contraction ratio the pressure distribution stayed quite constant along the chamber axis for each load point before entering the nozzle section.

Although the propellants were injected at very high momentum flux ratios, no unfavorable behavior in the flame anchoring or combustion stability were observed.

The characteristics of flame visualization with UV radiation, filtered to OH* emission, and blue radiation could be compared and contrasted. The trends in flame topology with injection conditions from both imaging types were consistent, although the measured values differed slightly due to differing intensity gradients at the flame boundaries, affecting the threshold-based edge detection. OH* radiation has stronger gradients at flame edges and less variation in absolute intensity between operating conditions, resulting in far lower uncertainty in the identification of the flame boundaries. OH* radiation has a high degree of self-absorption, whereas blue radiation provides a true line-of-sight integrated image and can be processed for example with the inverse Abel transformation to

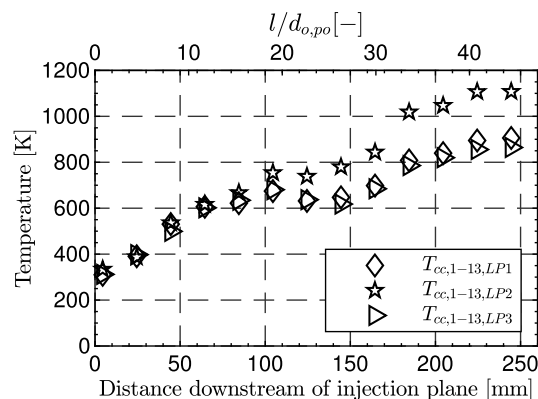


Fig. 18. Temperature distribution of hot gas thermocouples downstream of injection plane.

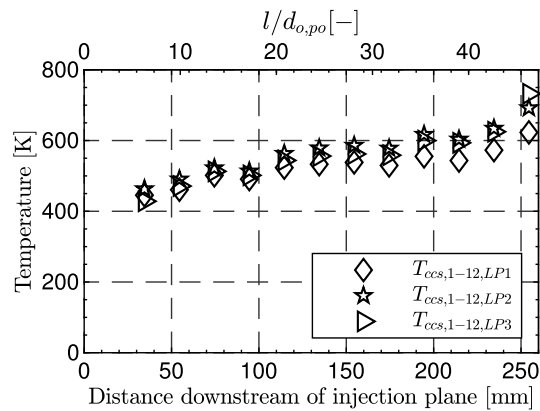


Fig. 19. Temperature distribution of thermocouples in chamber wall downstream of injection plane.

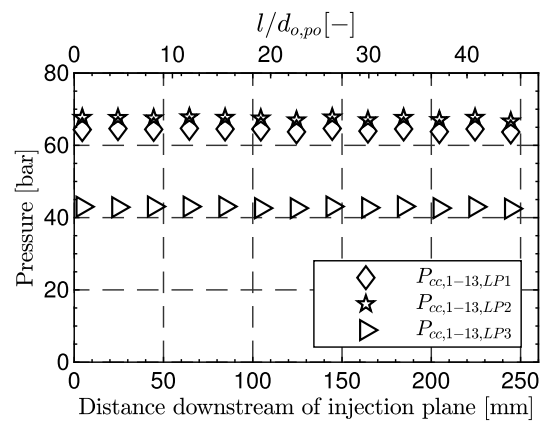


Fig. 20. Pressure distribution in chamber downstream of injection plane.

provide an emulated cross-sectional view of the flame. The simultaneous use of both methods therefore provides complementary information on the topology of the flame.

Author statement

Jan Martin: Formal analysis, Investigation, Writing - Original Draft, Writing - Review & Editing, Visualization.

Wolfgang Armbruster: Writing - Original Draft, Writing - Review & Editing.

Robert Stützer: Writing - Original Draft, Writing - Review & Editing, Resources.

Stephan General: Investigation, Writing - Original Draft, Resources.

Bernhard Knapp: Investigation, Resources.

Dmitry Suslov: Investigation.

Justin Hardi: Conceptualisation, Investigation, Data Curation, Supervision, Funding acquisition, Project administration, Writing - Review & Editing.

Declaration of competing interest

The authors declare that they have no known competing financial interests or personal relationships that could have appeared to influence the work reported in this paper.

Acknowledgments

The work is associated with DLR project of Advanced Methods for reusable Aerospace vehicle DEsign Using artificial intelligence and interdisciplinary numerical Simulation (AMADEUS). Co-funding was provided by ESA in the framework of the Technology Development Element programme (TDE). The authors would also like to thank the crew of the P8 test bench. Thanks also to Alex Grebe for his assistance in performing the experiments.

References

- [1] D.K. Huzel, D.H. Huang, *Modern Engineering for Design of Liquid-Propellant Rocket Engines (Revised and Enlarged Edition)*, American Institute of Aeronautics and Astronautics, 1992.
- [2] G.P. Sutton, O. Biblarz, *Rocket Propulsion Elements*, eighth ed., John Wiley & Sons, New York, 2010.
- [3] A. Frank, D. Regenbrecht, The test centre Lampoldshausen and its role in Ariane 6 and beyond, in: Space Ops 2016 Conference, Daejeon, Korea, 2016, <https://doi.org/10.2514/6.2016-2503>.
- [4] T. Fuhrmann, B. Mewes, F.D. Moya, M. Horstmann, FLPP ETID: enabling technologies for future European upper stage engines, in: 7th European Conference for Aeronautics and Aerospace Sciences (EUCASS) 2017, 2017. Mailand.
- [5] H. Kawashima, T. Kobayashi, K. Okita, Progress of LE-9 engine development, in: AIAA Propulsion and Energy Forum, 2018 Joint Propulsion Conference, 2018, <https://doi.org/10.2514/6.2018-4458>. AIAA 2018-4458, Cincinnati, OH.
- [6] V. Rachuk, N. Titkov, The first Russian LOX-LH2 expander cycle LRE: RD0146, in: 42nd AIAA/ASME/SAE/ASEE Joint Propulsion Conference & Exhibit, American Institute of Aeronautics and Astronautics, 2006. AIAA 2006-4904, Sacramento, CA, doi: 10.2514/6.2006-4904.
- [7] W. Wang, D. Zheng, G. Qiao, Development status of the cryogenic oxygen hydrogen YF-77 engine for long-march 5, in: 64th International Astronautical Congress (IAC), 2013. Beijing, China.
- [8] J. Hulka, J.J. Hutt, Instability phenomenology and case studies: instability phenomena in liquid oxygen/hydrogen propellant rocket engines, in: V. Yang, W. E. Anderson (Eds.), *Liquid Rocket Engine Combustion Instability*, American Institute of Aeronautics and Astronautics, Washington, DC, 1995, pp. 39–71, <https://doi.org/10.2514/5.9781600866371.0039.0071>. Ch. 2.
- [9] D.I. Suslov, J.S. Hardi, M. Oswald, Full-length visualisation of liquid oxygen disintegration in a single injector sub-scale rocket combustor, *Aero. Sci. Technol.* 86 (2019) 444–454, <https://doi.org/10.1016/j.ast.2018.12.027>.
- [10] J.S. Hardi, *Experimental Investigation of High Frequency Combustion Instability in Cryogenic Oxygen-Hydrogen Rocket Engines*, Ph.D. thesis, The University of Adelaide, Australia, 2012.
- [11] G. Schmidt, *Technik der Flüssigkeits-Raketentriebwerke*, DaimlerChryslerAerospace, Taufkirchen, 1999.
- [12] N. Yatsuyanagi, Establishment of design method for liquid hydrogen regenerative cooling combustor of LOX/Hydrogen rocket engine, *Trans. Jpn. Soc. Aeronaut. Space Sci.* 51 (174) (2009) 259–266, <https://doi.org/10.2322/tjsass.51.259>.
- [13] J.C. Oefelein, Mixing and combustion of cryogenic oxygen-hydrogen shear-coaxial jet flames at supercritical pressure, *Combust. Sci. Technol.* 178 (1–3) (2006) 229–252, <https://doi.org/10.1080/00102200500325322>.
- [14] A. Urbano, L. Selle, G. Staffelbach, B. Cuenot, T. Schmitt, S. Ducruix, S. Candel, Exploration of combustion instability triggering using large eddy simulation of a multiple injector liquid rocket engine, *Combust. Flame* 169 (July 2016) 129–140, <https://doi.org/10.1016/j.combustflame.2016.03.020>.
- [15] M. Lempe, P. Gerlinger, M.J. Seidl, M. Aigner, Unsteady high-order simulation of a liquid oxygen/gaseous hydrogen rocket combustor, *J. Propul. Power* 31 (6) (2015) 1715–1726, <https://doi.org/10.2514/1.B35726>.
- [16] T. Schmitt, G. Staffelbach, S. Ducruix, S. Gröning, J. Hardi, M. Oswald, Large-eddy simulations of a sub-scale liquid rocket combustor: influence of fuel injection temperature on thermo-acoustic stability, in: 7th European Conference for Aeronautics and Aerospace Sciences, (EUCASS) 2017, Milano, Italy, 2017, <https://doi.org/10.13009/EUCASS2017-352>.
- [17] D. Banuti, M. Raju, P.C. Ma, M. Ihme, J.-P. Hickey, Seven questions about supercritical fluids – towards a new fluid state diagram, in: 55th AIAA Aerospace Sciences Meeting, 2017, <https://doi.org/10.2514/6.2017-1106>. AIAA 2017-1106, Grapevine, TX.
- [18] S. Pohl, M. Jarczyk, M. Pfützner, B. Rogg, Real gas cfd simulations of hydrogen/oxygen supercritical combustion, *Prog. Propul. Phys.* 4 (2013) 583–614.
- [19] O. Knab, H. Riedmann, B. Ivancic, C. Höglaue, M. Frey, T. Aichner, Consequences of Modeling Demands on Numerical Rocket Thrust Chamber Flow Simulation Tools, 2019, <https://doi.org/10.1051/eucass/201911317>.
- [20] B. Ivancic, W. Mayer, Time-and length scales of combustion in liquid rocket thrust chambers, *J. Propul. Power* 18 (2) (2002) 247–253, <https://doi.org/10.2514/2.5963>.
- [21] M.M. Masquelet, *Simulations of a Sub-Scale Liquid Rocket Engine: Transient Heat Transfer in a Real Gas Environment*, Georgia Institute of Technology, Dissertation, 2006.
- [22] N. Tani, K. Ogura, N. Yamanishi, H. Negishi, H. Sunakawa, T. Kobayashi, An End-To-End High Fidelity Numerical Simulation of the LE-X Engine - Influence of Coolant Leakage on Engine Power Balance -. doi:10.2514/6.2013-3907.
- [23] V.P. Zhukov, D.I. Suslov, Measurements and modelling of wall heat fluxes in rocket combustion chamber with porous injector head, *Aero. Sci. Technol.* 48 (2016) 67–74, <https://doi.org/10.1016/j.ast.2015.10.021>.
- [24] P.C. Ma, H. Wu, M. Ihme, J.-P. Hickey, Nonadiabatic flamelet formulation for predicting wall heat transfer in rocket engines, *AIAA J.* 56 (6) (2018) 2336–2349, <https://doi.org/10.2514/1.J056539>.
- [25] D. Eiringhaus, H. Riedmann, O. Knab, Definition and Evaluation of Advanced Rocket Thrust Chamber Demonstrator Concepts, Springer International Publishing, 2021, pp. 407–419, https://doi.org/10.1007/978-3-030-53847-7_26. https://doi.org/10.1007/978-3-030-53847-7_26.
- [26] N. Perakis, D. Rahn, O.J. Haidn, D. Eiringhaus, Heat transfer and combustion simulation of seven-element o₂/ch₄ rocket combustor, *J. Propul. Power* 35 (6) (2019) 1080–1097, <https://doi.org/10.2514/1.B37402>.
- [27] M. Wohlhüter, V.P. Zhukov, J. Sender, S. Schlechtriem, Analysis of the laser ignition of methane/oxygen mixtures in a sub-scale rocket combustion chamber, *CEAS Space J.* 9 (2) (2017) 211–225, <https://doi.org/10.1007/s12567-016-0143-3>.
- [28] M. Schulze, T. Sattelmayer, Linear stability assessment of a cryogenic rocket engine, *Int. J. Spray Combust. Dyn.* 9 (4) (2017) 277–298.
- [29] L. Hakim, A. Ruiz, T. Schmitt, M. Boileau, G. Staffelbach, S. Ducruix, B. Cuenot, S. Candel, Large eddy simulations of multiple transcritical coaxial flames submitted to a high-frequency transverse acoustic modulation, *Proc. Combust. Inst.* 35 (2) (2015) 1461–1468, <https://doi.org/10.1016/j.proci.2014.05.142>.
- [30] R. Kaess, S. Koeglmeier, T. Sattelmayer, M. Schulze, M. Oswald, J. Hardi, Hf combustion stability - research activities in Germany, in: *Space Propulsion 2016*, Italy, Roma, 2016.
- [31] A. Urbano, Q. Douasbin, L. Selle, G. Staffelbach, B. Cuenot, T. Schmitt, S. Ducruix, S. Candel, Study of flame response to transverse acoustic modes from the les of a 42-injector rocket engine, *Proc. Combust. Inst.* 36 (2) (2017) 2633–2639, <https://doi.org/10.1016/j.proci.2016.06.042>.
- [32] S. K. Beinke, J. S. Hardi, D. T. Banuti, S. Karl, B. B. Dally, M. Oswald, Experimental and numerical study of transcritical oxygen-hydrogen rocket flame response to transverse acoustic excitation, *Proc. Combust. Inst.* 10.1016/j.proci.2020.05.027.
- [33] C. Laurent, G. Staffelbach, F. Nicoud, T. Poinso, Heat-release dynamics in a doubly-transcritical LO₂/LCH₄ cryogenic coaxial jet flame subjected to fuel inflow acoustic modulation, *Proc. Combust. Inst.* 10.1016/j.proci.2020.05.051.
- [34] M. Son, K. Radhakrishnan, Y. Yoon, J. Koo, Numerical study on the combustion characteristics of a fuel-centered pintle injector for methane rocket engines, *Acta Astronaut.* 135 (2017) 139–149, <https://doi.org/10.1016/j.actaastro.2017.02.005>.
- [35] S. Gröning, *Untersuchung selbstregulierter Verbrennungsinstabilitäten in einer Raketentriebkammer*, Ph.D. thesis, RWTH Aachen, Aachen, Germany, 2017.
- [36] M. Oswald, J. Smith, R. Branam, J. Hussong, A. Schik, B. Chehroudi, D. Talley, Injection of fluids into supercritical environments, *Combust. Sci. Technol.* 178 (2006) 49–100, <https://doi.org/10.1080/00102200500292464>.
- [37] W. Mayer, H. Tamura, Propellant injection in a liquid oxygen/gaseous hydrogen rocket engine, *J. Propul. Power* 12 (6) (1996) 1137–1148, <https://doi.org/10.2514/3.24154>.
- [38] A. Chemnitz, T. Sattelmayer, C. Roth, O. Haidn, Y. Daimon, R. Keller, P. Gerlinger, J. Zips, M. Pfützner, Numerical investigation of reacting flow in a methane rocket combustor: turbulence modeling, *J. Propul. Power* 34 (4) (2018) 864–877, <https://doi.org/10.2514/1.B36565>.
- [39] N. Perakis, O. J. Haidn, D. Eiringhaus, D. Rahn, S. Zhang, Y. Daimon, S. Karl, T. Horchler, Qualitative and Quantitative Comparison of RANS Simulation Results for a 7-Element GOX/GCH₄ Rocket Combustor. doi:10.2514/6.2018-4556.
- [40] J.S. Hardi, W.Z. Hallum, C. Huang, W.E. Anderson, Approaches for comparing numerical simulation of combustion instability and flame imaging, *J. Propul. Power* 32 (2) (2016) 279–294, <https://doi.org/10.2514/1.B35780>.

- [41] Y. Nunome, M. Takahashi, A. Kumakawa, K. Miyazaki, S. Yoshida, T. Onga, High-frequency flame oscillation observed at a coaxial lox/h₂ injector element, in: 44th AIAA/ASME/SAE/ASEE Joint Propulsion Conference & Exhibit 208, Hartford, Connecticut, 2008, <https://doi.org/10.2514/6.2008-4848>. AIAA Paper 2008-4848.
- [42] R. Woodward, S. Pal, S. Farhangi, R. Santoro, LOX/GH₂ shear coaxial injector atomization studies at large momentum flux ratios, in: 42nd AIAA/ASME/SAE/ASEE Joint Propulsion Conference & Exhibit, American Institute of Aeronautics and Astronautics, 2006, <https://doi.org/10.2514/6.2006-5203>.
- [43] M. Roa, D.G. Talley, Wave dynamic mechanisms in coaxial hydrogen/liquid^o-oxygen jet flames, *J. Propul. Power* 35 (2) (2019) 369–381, <https://doi.org/10.2514/1.B37079>.
- [44] J.S. Hardi, S.K. Beinke, M. Oschwald, B.B. Dally, Coupling of cryogenic oxygen-hydrogen flames to longitudinal and transverse acoustic instabilities, *J. Propul. Power* 30 (4) (2014) 991–1004, <https://doi.org/10.2514/1.B35003>.
- [45] S. Candel, G. Herding, R. Synder, P. Scoufflaire, C. Rolon, L. Vingert, M. Habiballah, F. Grisch, M. Pé alat, P. Bouchardy, D. Stepowski, A. Cessou, P. Colin, Experimental investigation of shear coaxial cryogenic jet flames, *J. Propul. Power* 14 (5) (1998) 826–834, <https://doi.org/10.2514/2.5346>.
- [46] S. Candel, M. Juniper, G. Singla, P. Scoufflaire, C. Rolon, Structure and dynamics of cryogenic flames at supercritical pressure, *Combust. Sci. Technol.* 178 (1–3) (2006) 161–192, <https://doi.org/10.1080/00102200500292530>.
- [47] W. Armbruster, J.S. Hardi, D. Suslov, M. Oschwald, Injector-driven flame dynamics in a high-pressure multi-element oxygen-hydrogen rocket thrust chamber, *J. Propul. Power* 35 (2019) 632–644, <https://doi.org/10.2514/1.B37406>.
- [48] B. Ivancic, H. Riedmann, M. Frey, Validation of turbulent combustion models for 3d-simulations of liquid h₂/o₂ rocket combustors, in: *Space Propulsion Conference*, 2012.
- [49] M. Masquelet, S. Menon, Large-eddy simulation of flame-turbulence interactions in a shear coaxial injector, *J. Propul. Power* 26 (5) (2010) 924–935, <https://doi.org/10.2514/1.48023>.
- [50] S. Fechter, T. Horschler, S. Karl, K. Hannemann, D. Suslov, J. Hardi, M. Oschwald, Efficient handling of cryogenic equation of state for the simulation of rocket combustion chambers, in: F. di Mare, A. Spinelli, M. Pini (Eds.), *Non-Ideal Compressible Fluid Dynamics for Propulsion and Power*, Springer International Publishing, 2020, pp. 19–30.
- [51] A. Lechtenberg, P. M. Gerlinger, Numerical investigation of combustion instabilities in a rocket combustion chamber with supercritical injection using a hybrid rans/les method, in: *AIAA Scitech 2020 Forum*. doi:10.2514/6.2020-1162.
- [52] J. Lux, O. Haidn, Flame stabilization in high-pressure liquid oxygen/methane rocket engine combustion, *J. Propul. Power* 25 (1) (2009) 15–23, <https://doi.org/10.2514/1.36852>.
- [53] Steady-state high pressure lox/h₂ rocket engine combustion, *Aero. Sci. Technol.* 11 (1) (2007) 39–47, <https://doi.org/10.1016/j.ast.2006.08.007>.
- [54] A. Habertzell, D. Suslov, G. Brümmer, A. Frank, M. Oschwald, European technology test facility for high pressure combustion P8. 20 years research and technology development, in: *Deutscher Luft- und Raumfahrtkongress (DLRK) 2016*, 2016. Braunschweig, Germany.
- [55] T. Fiala, T. Sattelmayer, S. Gröning, J. Hardi, R. Stützer, S. Webster, M. Oschwald, Comparison between excited hydroxyl radical and blue radiation from hydrogen rocket combustion, *J. Propul. Power* 33 (2) (2017) 490–500, <https://doi.org/10.2514/1.B36280>.
- [56] T. Fiala, T. Sattelmayer, On the use of oh* radiation as a marker for the heat release rate in high-pressure hydrogen-oxygen liquid rocket combustion, in: 49th AIAA/ASME/SAE/ASEE Joint Propulsion Conference & Exhibit, American Institute of Aeronautics and Astronautics, 2013, <https://doi.org/10.1063/1.1692590>.
- [57] T. Fiala, *Radiation from High Pressure Hydrogen-Oxygen Flames and its Use in Assessing Rocket Combustion Instability*, Ph.D. thesis, Technical University of Munich, Munich, Germany, 2015.
- [58] T. Kathrotia, M. Fikri, M. Bozkurt, M. Hartmann, U. Riedel, C. Schulz, Study of the h + o + m reaction forming oh*: kinetics of oh* chemiluminescence in hydrogen combustion systems, *Combust. Flame* 157 (7) (2010) 1261–1273, <https://doi.org/10.1016/j.combustflame.2010.04.003>.
- [59] M.D. Leo, A. Saveliev, L.A. Kennedy, S.A. Zelepouga, Oh and ch luminescence in opposed flow methane oxy-flames, *Combust. Flame* 149 (4) (2007) 435–447, <https://doi.org/10.1016/j.combustflame.2007.01.008>.
- [60] P.J. Padley, The origin of the blue continuum in the hydrogen flame, *J. Trans. Faraday Soc.* 56 (1960) 449–454.
- [61] A. Gaydon, *The Spectroscopy of Flames*, Chapman and Hall, London, 1957.
- [62] J.d.P. Peter Atkins, *Atkins' Physical Chemistry*, Oxford University Press, 2014. https://www.ebook.de/de/product/21743493/peter_atkins_julio_de_paula_atkins_physical_chemistry.html.
- [63] J. Luque, D.R. Crosley, Transition probabilities in the $a^2\sigma^+-x^2\pi_i$ electronic system of oh, *J. Chem. Phys.* 109 (2) (1998) 439–448, <https://doi.org/10.1063/1.476582>.
- [64] E.W. Hansen, P.-L. Law, Recursive methods for computing the abel transform and its inverse, *J. Opt. Soc. Am. A* 2 (4) (1985) 510, <https://doi.org/10.1364/josaa.2.000510>.
- [65] D. Kendrick, G. Herding, P. Scoufflaire, C. Rolon, S. Candel, Effects of a recess on cryogenic flame stabilization, *Combust. Flame* 118 (3) (1999) 327–339, [https://doi.org/10.1016/s0010-2180\(98\)00168-0](https://doi.org/10.1016/s0010-2180(98)00168-0).